Noise mapping with the PE method
– a case study from interior Norway

Knut Waagan

FFI Forsvarets
forskningsinstitutt

Noise mapping with the PE method
– a case study from interior Norway

Knut Waagan

Norwegian Defence Research Establishment (FFI)

13. oktober 2015

Keywords

Støy

Akustikk

Beregning

Metereologi

Skytefelt

Approved by

Eirik Svinsås   Project Manager

Jon. E. Skjervold   Director

English summary

The Norwegian Armed Forces presently use the software Milnoise for mapping acoustic noise from their shooting- and practice ranges. Research and development on computational methods for outdoor sound propagation have focused largely on noise from traffic and industry, and Milnoise is predominantly based on those methods. Noise from heavier weapons and explosions differs from traffic noise in its low frequency content and longer range. This report is part of a project aiming to improve computational methods for such noise, thereby enabling more accurate prediction.

At long distances it is known that sound propagation is strongly influenced by the weather conditions, with effects up to tens of dB. We have implemented a so-called parabolic equation (PE) method that can take into account detailed knowledge of weather conditions. PE methods are well established computational techniques, and much used for outdoor acoustics as well as other wave propagation phenomena. We have emphasised efficient implementation, i.e. short computation time. Even so, the increased level of detail compared to current Milnoise comes at a computational cost. In this report we demonstrate how the PE method can handle a realistic scenario with firing of an M109 howitzer at a practice range in Southern Norway.

Since the PE method is a relatively precise acoustics model, much of the uncertainty in the resulting noise maps is related to the quality of the input weather and ground data. Over long distances it is very challenging to obtain good weather data. Ideally one should know the temperature and wind in rather large detail up to 2000 m altitude and in a radius of 20 km around the shooting range. The weather model in this report uses local data from weather stations that are distributed in or near the shooting range at different altitudes.

Sammendrag

Forsvaret bruker i dag programvaren Milnoise for å kartlegge akustisk støy fra skyte- og øvingsfelt. Forskning på og utvikling av regnemetoder for utendørs lydutbredelse har hatt hovedfokuset på støy fra trafikk og industri, og Milnoise baserer seg i stor grad på de samme metodene. Lyd fra tyngre våpen og eksplosjoner skiller seg imidlertid fra trafikkstøy ved blant annet *lav frekvens* og lang rekkevidde. Rapporten er del av et prosjekt med mål å forbedre regnemetodene for slik støy, og dermed øke nøyaktigheten i støykartleggingen.

På lang avstand er det kjent at lydutbredelsen er sterkt påvirket av værforhold, med lokale utslag på flere titalls desibel. Vi har implementert en regnemetode som kan ta i bruk detaljert kunnskap om været. Metoden er en såkalt 'parabolic equation method'. PE-metoder er anerkjent og mye brukt i utendørsakustikk og for andre bølgefenomener. Vi har lagt vekt på effektiv implementasjon, dvs. kort regnetid, men det vil uansett være en regnekostnad knyttet til det økte detaljnivået sammenliknet med Milnoise. I denne rapporten viser vi hvordan regnemetoden kan håndtere et realistisk scenario med skytestøy fra M109 155 mm felthaubits på Rena øvingsfelt.

Siden PE-metoden er en relativt presis akustikkmodell, vil mye av usikkerheten i det resulterende støykartet komme fra input-dataene, det vil si vær og bakke-dataene. Over lange avstander er det svært krevende å få presise værdata. Ideelt sett bør man hele tiden vite temperatur og vind nokså detaljert opp til et par tusen meter og i en radius av et par mil rundt skytefeltet. I denne rapporten benytter vi lokale værstasjoner plassert i og nær Rena skytefelt i ulike høyder.

Contents

1 Introduction

Low frequency acoustic noise from military training can propagate long distances due to the strength of the sources and the low atmospheric dissipation. At long distances, refraction due to weather becomes important, and the resulting noise variability can amount to tens of dB, see [12]. In addition to atmospheric conditions, outdoor sound propagation is strongly influenced by ground conditions. At low frequencies, the ground interaction is particularly challenging to model. The majority of research in computational outdoor acoustics has been concerned with traffic and industrial noise, which, compared to artillery noise, is less far ranging and has less low frequency content.

The software Milnoise is currently used by the Norwegian Defence to predict noise around training facilities. Being based on traffic noise, it has limited abilities for sound below 100 Hz, and particularly below 25 Hz. This report is about a method that can compute noise propagation in the range 1-100 Hz, hence potentially improving Milnoise. The strategy is to allow for general atmospheric data, quite general topography, and to incorporate an adequate ground model. Unfortunately, the generality comes at a computational cost compared to present day Milnoise.

In order to demonstrate the practical use of the new method, we will apply it to a test case from the training ground at Rena. Realistic weather, topography and ground conditions will be used as input to the model, and the output will be a map of noise levels. The terrain at Rena is rather complicated, which, in particular, makes the modelling of atmospheric conditions very challenging.

2 The model

We will employ the linear Parabolic Equation (PE) model for sound propagation as presented and tested in a previous report ([14]). It can be briefly characterised as a simplified Helmholtz equation. This section contains a summary of the PE propagation model, followed by descriptions of the weather data and the ground interaction model.

2.1 Basic quantities

We consider a point source situated at a height z_s above ground, and seek to determine the sound pressure as a function of time, location and height. Cylindrical symmetry around the source location is assumed in the calculations, as a full three-dimensional model is likely not worth the significant extra cost. Hence the sound pressure p is considered a function of time, the horizontal distance r, referred to as range, and height above ground z.

Fourier transforming in time, we get the complex pressure $p_f(r, z)$ for each frequency f. The sound pressure level is defined as

$$L_p(f) = 10 \log_{10} |p_f/p_{\text{ref}}|^2, \quad p_{\text{ref}} = 2 \times 10^{-5} \text{ Pa.} \tag{2.1}$$

For a point source it can be decomposed as

$$L_p(f) = L_0(f) - 10 \log_{10}(R/R_0)^2 + \Delta L_f, \tag{2.2}$$

where L_0 is the sound pressure level in a homogeneous free atmosphere at some reference distance R_0, the second term is the geometric loss, and ΔL_f is called the relative sound level. Hence, ΔL_f contains all information about refraction, terrain and ground effects and is independent of the source. Equation (2.2) is only valid for linear sound propagation. Linearity may not hold near the source, but the nonlinear effects are incorporated in the source data L_0, as described in [5].

The goal is to determine the sound exposure level (SEL) of a signal given by

$$\text{SEL} = 10 \log_{10} t_{\text{ref}}^{-1} \int |p/p_{\text{ref}}|^2 \, dt = 10 \log_{10} t_{\text{ref}}^{-1} \int |p_f/p_{\text{ref}}|^2 \, df, \tag{2.3}$$

with the reference time $t_{\text{ref}} = 1$ s. Because of this identity, and because source data are given in the frequency domain, all the calculations can be performed in the frequency domain. Frequencies are sampled evenly on a logarithmic scale, with 12th octaves being the finest resolution (i.e. $f_j = 2^{j/12} f_0$ for integer j). We then use a standard trapezoidal rule to approximate (2.3). Sound source data are typically given for third octave bands.

The weather data maps to predicted noise via the sound speed c. In this study, c depends on air temperature T according to the relation

$$c = 340 \text{ m/s} \sqrt{\frac{T}{288.15\text{K}}}. \tag{2.4}$$

The horizontal wind speed component u in the direction of propagation defines the effective sound speed $c_{\text{eff}} = c + u$. We use the so-called effective sound speed approximation, which consists of an unmoving atmosphere with c replaced by c_{eff}. By wave number k we therefore refer to the effective wave number $2\pi f/c_{\text{eff}}$, strictly speaking.

The sound waves will interact with the ground, and ideally we would include wave motion in the ground as a part of the model. In outdoor acoustics, it is very common to instead model the ground as an impedance surface, meaning that the complex pressure satisfies

$$\frac{\partial p_f}{\partial z} = -\frac{ik}{Z} p_f, \tag{2.5}$$

at the ground surface, with the specific impedance Z depending strongly on frequency. It is useful to also define the admittance $\beta = 1/Z$.

2.2 Parabolic propagation model

The topography is represented by a piecewise linear function of range. For each topography section, we can hence write the altitude as $H(r) = H_0 + C(r - r_0)$. Sound propagation is then modelled with the wide angle Parabolic Equation:

$$\Psi_r + \frac{i}{2k_a} L_1 \Psi + \frac{1}{4k_a^2} L_1 \Psi_r + \frac{i}{k_a} C \Psi_{zr} = 0, \tag{2.6}$$
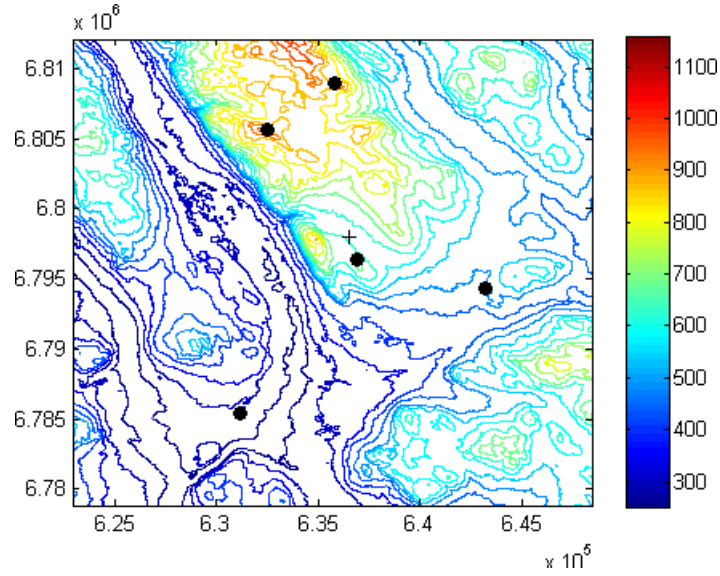
Figure 2.1   The location of the sound source (cross), and of the five automatic weather stations (circles).

where the differential operator L_1 is defined by

$$L_1\Psi = (C^2 + 1)\Psi_{zz} - 2ik_a C\Psi_z + (k^2 - k_a^2)\Psi. \tag{2.7}$$

The complex pressure can be retrieved by the relation

$$p_f(r, z) = \Psi(r, z)e^{ik_a r}/\sqrt{r}.$$

We let the constant k_a equal the wave number at ground level (hence it changes with each range section). Note that we let z denote height above ground. This notation differs from the presentation in the text book [9]. Equation (2.6) is a special case of the GTPE for general smooth terrain introduced in [8].

The computational domain is closed at the bottom with the impedance surface condition (2.5). At the top, the computational domain must be artificially truncated, and in this report we truncate at height $z_{\text{top}} = 1.5$ km. An absorption layer of thickness 50 wavelengths is added above z_{top} as described in [15]. In the parabolic approximation, we need a source model (a 'start-up field') for all heights z at range $r = 0$. Equations G.75 and G.79 from [9] are chosen, as they gave good results for low frequencies in [15].

2.3   Weather model

In and around the Rena practice range there are four automatic weather stations (AWSs) that register wind and temperature every ten minutes. They are quite spread out in the terrain, as seen in Figure 2.1, and also spread out altiduninally, with respectively 260 (Risskogen), 460 (Østre Æra), 640 (Tørråsen) and 960 (Fagerfjellet) meters above sea level. Formerly there was an AWS
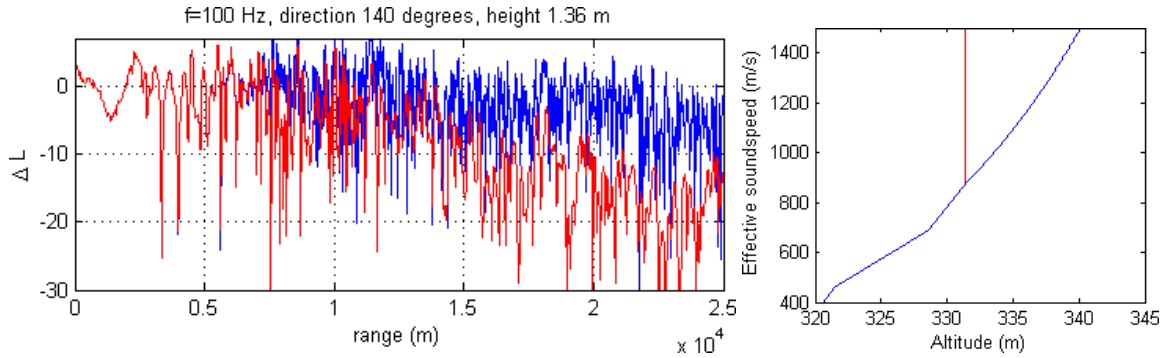
*Figure 2.2   Wind models above weather stations: Constant versus logarithmic. The frequency
$f = 100$ Hz is considered. Left: Relative sound level by range, right: Effective sound
speed profiles (the red curve is partially hidden by the blue curve).*

at 900 m (Løsetknubben, the northernmost one), which was recently replaced by the one at 960 m.
This yields effective sound speed c_K at four altitudes h_K, if we assume that wind and temperature
only varies with altitude h. Interpolating between the heights h_k, we end up with an effective
sound speed profile $c_{\text{eff}}(h)$.

The underlying horizontal homogeneity assumption was demonstrated to be reasonable in observations at Finnskogen presented in [3], although they do note an exception for temperature inversions
in terrain depressions. The terrain was more moderate there than at Rena.

Above and below the AWSs we lack data. We are not aware of any commonly accepted strategy
for extrapolating over terrain nor such large scales, and choose to extrapolate with a constant effective sound speed in both directions. We have however experimented with alternative strategies,
an example of which is shown in Figure 2.2. Above the highest weather station, a logarithmic
shape is used, which corresponds to a wind strength increasing with height. We consider this
wind profile a worst case scenario. We observe clear discrepancies up to 10-15 dB. This example
demonstrates that more research is needed on how to model the wind profile up to about 2000 m
altitude. It is encouraging, however, that the AWS data are sufficient up to about 7 km range.

In [13], we obtained weather data from a different source. A weather forecast snapshot of the
effective sound speed profile was used as input to the PE model. This study also confirmed that
data above the weather stations can be important, even noting downward refraction in the upwind
direction caused by a jet feature in the wind field. The study also suggested that the surface layer
up to 100 m or so above ground might be important. The horizontal homogeneity assumption
was not entirely accurate about the wind field, but still useful, especially with proper treatment
of the surface layer. It should be mentioned that the weather forecast has one major disadvantage
compared to the AWS model: It uses an oversimplified topography, and should therefore only be
used for theoretical studies, and not actual sound prediction (unless some additional meso-scale
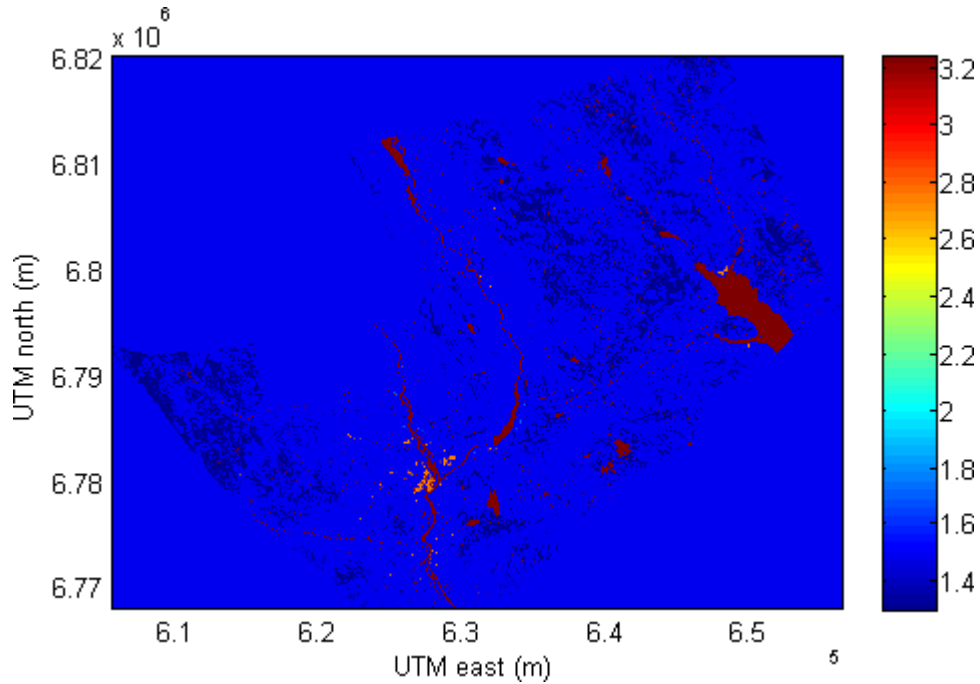modelling is introduced).

Figure 2.3   Map of $\log_{10}|Z|$ *for 64 Hz. NGI classification.*

The AWS data are provided every ten minutes, and are temporal averages. At small spatial scales, weather conditions will fluctuate much faster, due to turbulence. The only way presently to include these fluctuations is with computationally expensive stochastic methods. The papers [17] and [18] concluded that averaged weather profiles had predictive value even in a turbulent atmosphere. These works and others on this issue have been limited to flat, homogeneous terrain. An important known effect of small scale fluctuations, more precisely fluctuations on the scale of one wavelength, is the scattering of acoustic energy into shadow regions. In practice, this is taken into account by setting a lower bound on the relative sound pressure level ΔL. No simple formula exists for such a bound even in flat terrain, hence small scale fluctuations are ignored in this study.

2.4   Ground model

The ground impedance values Z in the boundary condition (2.5) are calculated following [19], as given in equations (C.9-11) in [9]. This requires knowledge of resistivity σ of and porosity Ω. Ground classification of the Rena area is provided by NGI as described in [6, 4]. There are seven surface classes, each with fixed values of σ and Ω. The most common ground type at Rena is forest/grassland. Forest is often interspersed with softer marshland. Water bodies are small except for a lake in the east. An example map is provided in Figure 2.3, which shows the logarithm of the magnitude of impedance $\log_{10}|Z|$. Snow cover is not considered in this study, but it should be noted that it is well-known to have an effect on sound levels.
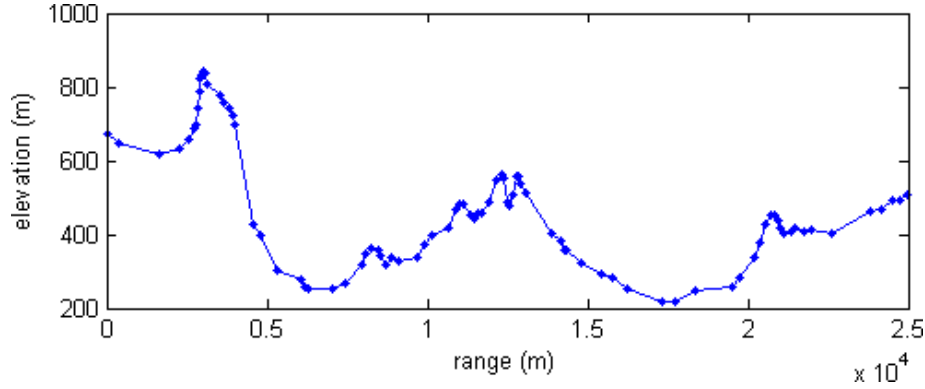
Figure 3.1   Example of data reduced topography.

3   Solution algorithm

The basic model and the numerical solution algorithm was described in [14]. This section describes modifications of the solution algorithm that allows efficient handling of realistic data.

3.1   Reduction of range-dependence

The Crank-Nicolson method that we use is most efficient for range-independent data as pointed out in [10]. As a compromise we divide the domain into reasonably long *range sections* with fixed slope, impedance and sound speed profile. An example topographic profile is shown in Figure 3.1. We achieve this by approximating the original terrain curve $H(r)$ with a piecewise linear curve such that the number of nodes is small. The approximation is chosen in the following way: We start with $H_0 = h\{0, r_{\text{end}}\}$, the linear interpolant between the two end points $r = 0$ and r_{end}. Then, in the first iteration find $r_1 = \arg\max |H - H_0|$. This yields the linear interpolant H_1 with three nodes $H_1 = h\{0, r_1, r_{\text{end}}\}$. For the second iteration find $r_2 = \arg\max |H - H_1|$ et cetera. We terminate the iteration once $\max |H - H_n| < 5$ m.

Note that for each iteration step, it is only necessary to interpolate between three range points, which allows for efficient implementation. In practice though, this algorithm only takes up a small fraction of the total computational time.

In order to take advantage of the reduced topography representation we also need to reduce the ground admittance and weather data. We propose to use average admittance values for each linear section. Our weather model consists of an effective sound speed profile c_{eff} that depends only on altitude (i.e. $H(r) + z$). Hence also c_{eff} is range-dependent, and must be reduced to depend only on z within each range section. To that end, we choose the effective sound speed profile at the midpoint of the range section. This choice works well for the particular terrain under study, but more generally we recommend to set an upper bound on the section length and the altitude difference.
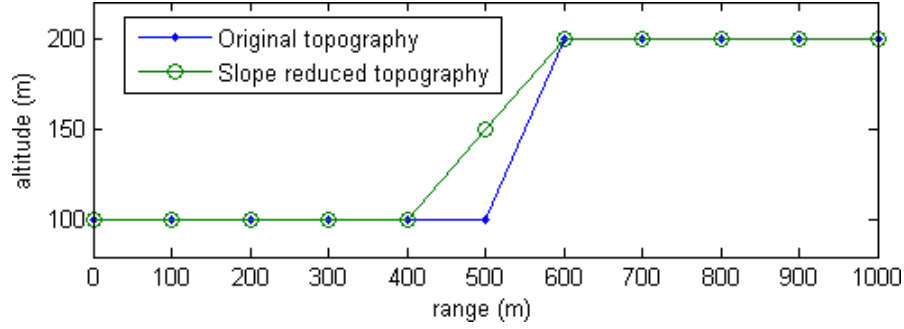
Figure 3.2   Illustration of the slope reduction algorithm.

3.2 Treatment of steep slopes

The PE algorithm becomes unstable for steep slopes. Therefore the slope has to be reduced at Rena in some places. The following algorithm is used: The height function $H(r)$ is replaced by

$$H_C = \min_{h \in L_C, h > H} h, \tag{3.1}$$

where L_C denotes all continuous functions h over $[0, r_{\text{end}}]$ such that $\|h'\|_\infty < C$. In other words, we want the smallest height profile $H_C > H$ such that H_C has slopes we can handle.

We approximate H_C as follows. Let H be given as linear interpolation between nodes

$$r_0, r_1, \ldots, r_k, \ldots, r_n.$$

Then we use the recursion formula

$$\begin{aligned}
H_C(r_0) &= H(r_0), \\
H_C(r_k) &= \max\{H(r_k),\, H_C(r_{k-1}) - C \times (r_k - r_{k-1})\} \quad \forall\, k \in \{1, 2, \ldots, n\}.
\end{aligned} \tag{3.2}$$

This forwards sweep reduces the downward slopes. A similar backwards sweep reduces the upward slopes. The algorithm (3.2) can only approximately solve the minimization problem (3.1) because it leaves the nodes r_k unchanged.

In the code this reduction of steepness is applied after the data reduction described in section 3.1. The maximum slope is set to 0.5, i.e. 30 degrees. A simple example is shown in Figure 3.2.

The idea here is that away from the reduced slopes, sound propagation is unaffected. We provide a numerical test in the Appendix. Obviously, if there is a steep upward slope near the source, shadowing effect may be improperly modelled, leading to an overestimation of sound level further afield. Likewise, a strong downward slope near the receiver may also lead to overestimated sound levels. It is not clear yet whether such cases will occur at Rena, but they will certainly be unusual.

3.3 Adaptive range truncation

The sound level near the ground is

$$L_p \approx L_W - 10 \log 4\pi r^2 + \Delta L, \tag{3.3}$$

following [9]. Dissipation and height-dependence are ignored here. When attenuation (negative of the last two terms) exceeds a certain level, say $L_{\min}$, it is no longer useful to prolong the integration to further range. This yields as a stopping criterion

$$|\Psi|^2 < 10^{L_{\min}/10} 4\pi r. \tag{3.4}$$

On the left hand side we plug in the maximum of $|\Psi|^2$ over $z < z_e$. As default values we set $L_{\min} = -100$ dB and $z_e = 1$ km.

3.4 Postprocessing

For single frequencies, cancellation effects cause the sound to virtually disappear at very localised ranges, see e.g. Figure 2.2. The location of these regions varies with the input data, hence the sound level may be severely underestimated locally. One strategy to avoid such underestimation is ensemble simulation which can be costly. Typically, averaging over a third octave frequency band is performed. In order to save computational time, we propose instead to postprocess sound level data for a single frequency with the aim to smooth out the minima.

The postprocessing algorithm is defined as follows: Let f be a real valued function of range r, and l a length. Then we can define the running average operator Q_l by

$$Q_l f(r) = l^{-1} \int_{r-l/2}^{r+l/2} f(\xi) d\xi. \tag{3.5}$$

Similarly, we can define the running maximum Q_l^∞ operator by

$$Q_l^\infty f(r) = \max_{r-l/2 < \xi < r+l/2} f(\xi). \tag{3.6}$$

Obviously, $Q_l^\infty f > f$, hence using this latter operator avoids underestimation completely. In the examples here we use the composition $Q_l Q_l^\infty$ with

$$l = \min(1, (32 \text{ Hz})/f) \times 250 \text{ m}.$$

Note that $l \le 250$ m. The postprocessing is applied to the quantity

$$E = |p_f|^2 / |p_{\text{free}}|^2 = 10^{\Delta L/10}. \tag{3.7}$$

In other words the relative sound level in dB after postprocessing is $10 \log_{10} Q_l Q_l^\infty E$.

Height (m)	285	490	715	900
Temperature (degrees Celsius)	-20.2	-15.7	-7.8	-9.6
Wind speed (m/s)	0.2	0.2	2.8	6.2
Wind direction (degrees)	62.9	12.7	285.1	323.5

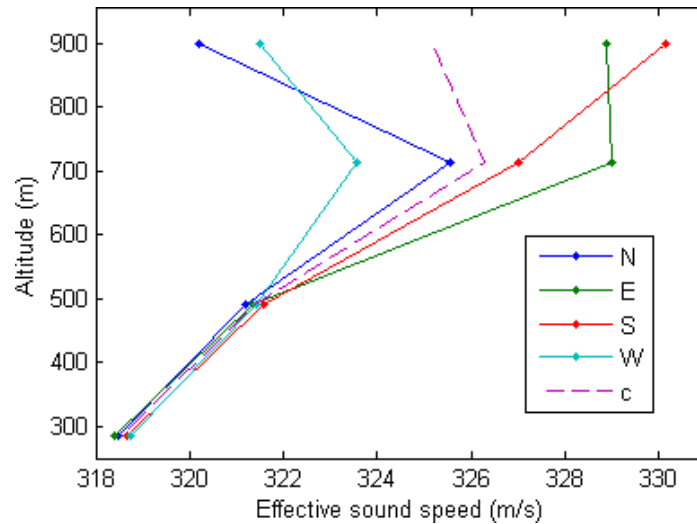*Table 4.1   Weather data for case study.*

Figure 4.1   Effective sound speed in four directions. The dashed line shows the regular sound speed.

4   Mapping case study

We consider a single source in this study. It is situated within the shooting range at Rena as plotted in Figure 2.1 (the UTM32 coordinates are 636.5 km east and 6798 km north). We will consider both attenuation of single frequencies and the SEL resulting from a specific weapon, an M109 155 mm howitzer. Weather data are from the weather stations on January 1st 2009 at 6pm as listed in Table 4.1. There was a strong temperature inversion typical of cold winter weather. There was some wind above the inversion directed towards the Southeast. Wind directions are given clockwise with $0°$ meaning wind from the North, $90°$ meaning wind from the East etc, as is standard for meteorological observations. Resulting effective sound speed profiles are plotted in Figure 4.1. Simulated sound levels along a transect for 100 Hz can be seen in Figure 4.2. At this frequency, ray paths are visible.

This section is structured as follows: First, some characteristic phenomena of the sound propagation is demonstrated by simulations. Next, noise maps are calculated with high sampling resolution in frequency and direction. These high resolution maps then serve as reference points for less detailed but more efficient calculations.
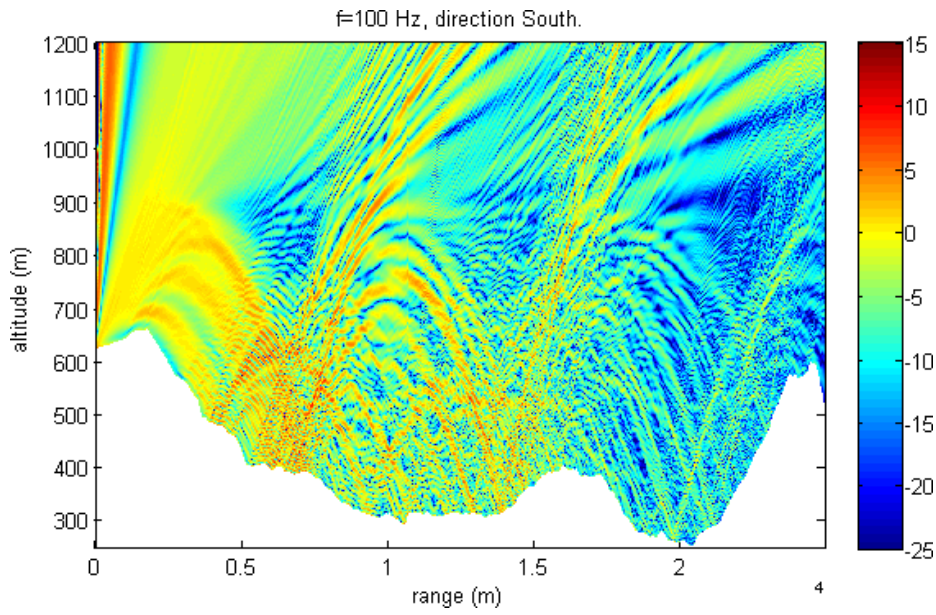
Figure 4.2   Relative sound level with vertical and horizontal dimensions for 100 Hz. Propagation direction towards the south.
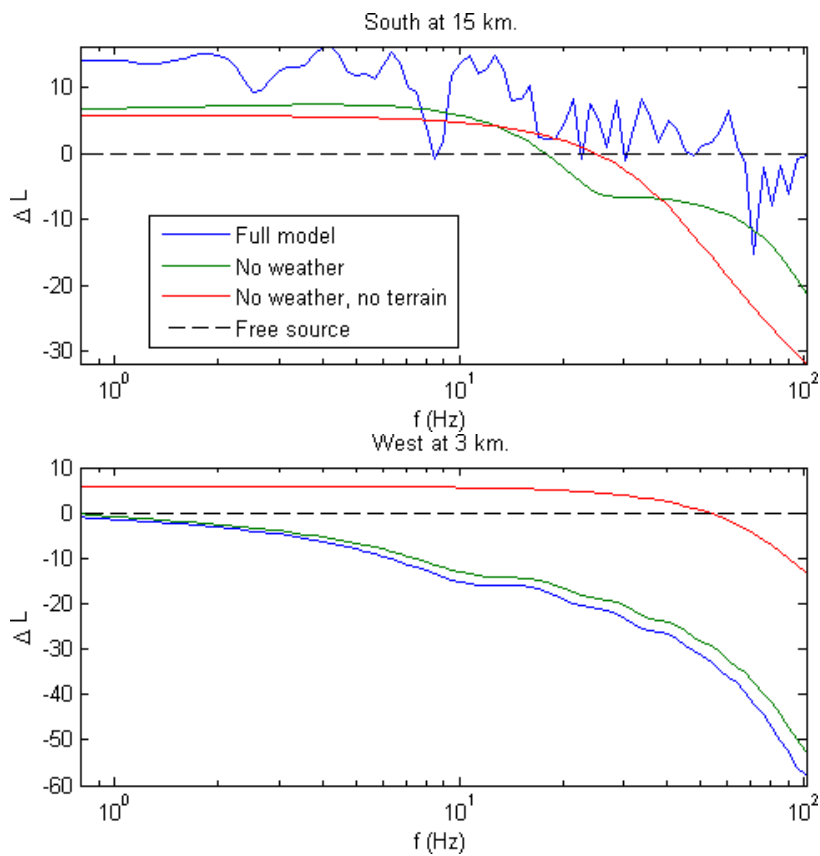

Figure 4.3   Top: Relative sound level spectrum at 15 km south from the source. Bottom: At 3 km west from the source. The dashed lines correspond to a free source.
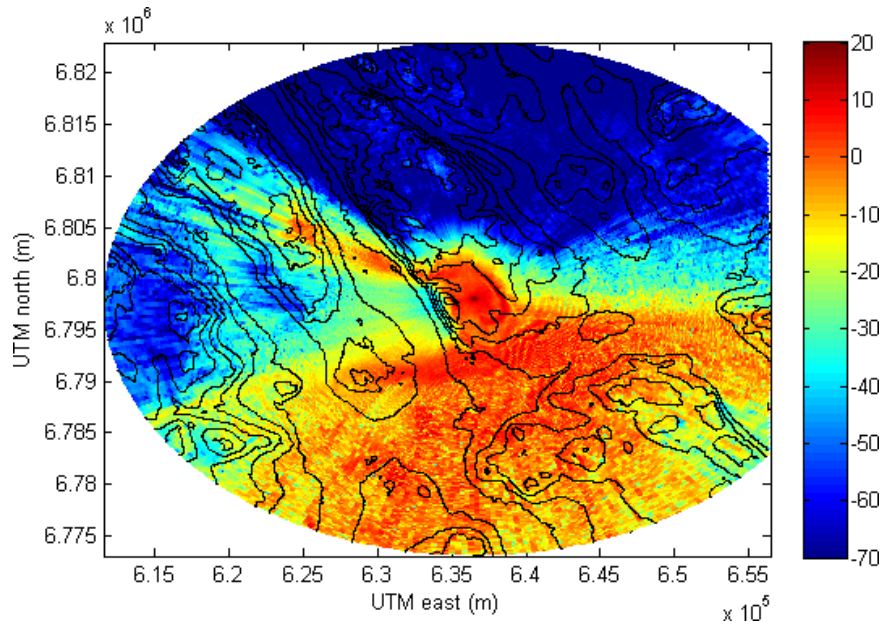
Figure 4.4   Relative sound level for 64 Hz.

4.1 Relative influence of model components

From the sound propagation simulations, it can be difficult to tell apart the relative importance of the physical effects. To clarify this, we include a comparison between the full model and simplified models. In Figure 4.3, the relative sound levels across the computed spectrum for various models are plotted. The simplest model consists of a free source, given by the dashed black line. The top plot shows the levels at 15 km south of the source. By including the ground interaction (using NGI ground data), we get the red line, with an approximate doubling of energy up to 10 Hz, and strong damping at 100 Hz. Including also topography (green line), has a complicated effect of up to about 10 dB. Finally, including the weather data, we get a strong downward refraction effect across the spectrum. We also note that downward refraction causes complicated small scale variation that is otherwise absent. The bottom plot shows a situation with strong terrain shadowing at 3 km west from the source. Including terrain reduces levels at all frequencies, and as expected, increasingly so with frequency. Weather appears unimportant in this case, possibly due to the crosswind propagation condition.

To summarise this section, we have demonstrated that weather, topography and ground interaction are all crucial model components at Rena.

4.2 High resolution noise map

As a reference noise map, we calculate relative sound level in 360 evenly distributed directions and for twelfth octaves from $2^{-1/3}$ (≈ 0.8) Hz to $2^{20/3}$ (≈ 101.6) Hz. Figure 4.4 shows relative sound levels ΔL for 64 Hz at 1.5 m above ground. The source is situated at around 700 m altitude, which is around the top of the temperature inversion. At this altitude, the wind becomes important,
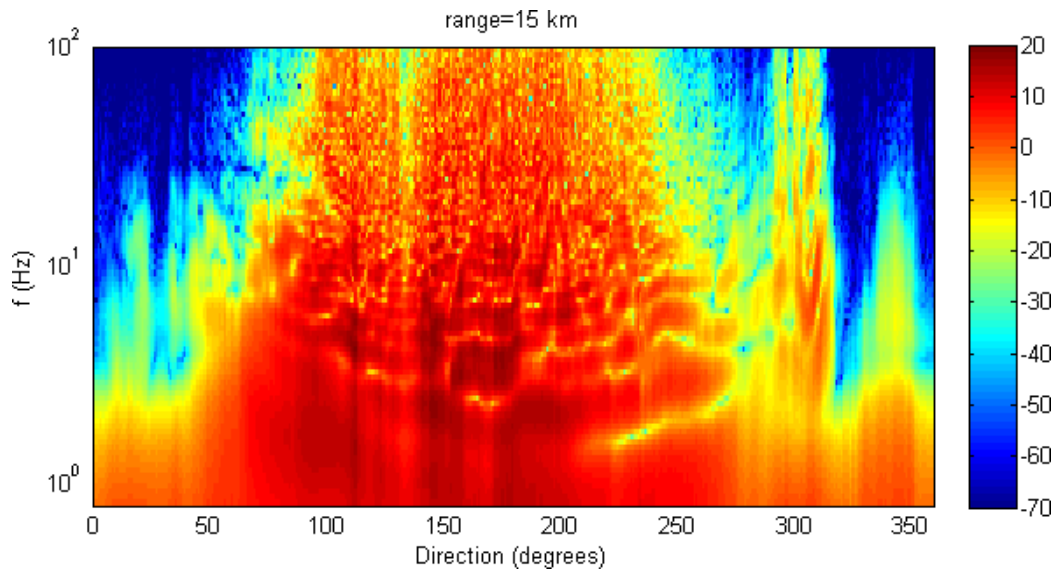
Figure 4.5   Relative sound level along a 15 km circle around the source for each frequency. Directions are given clockwise with zero degrees meaning sound propagation towards the North.
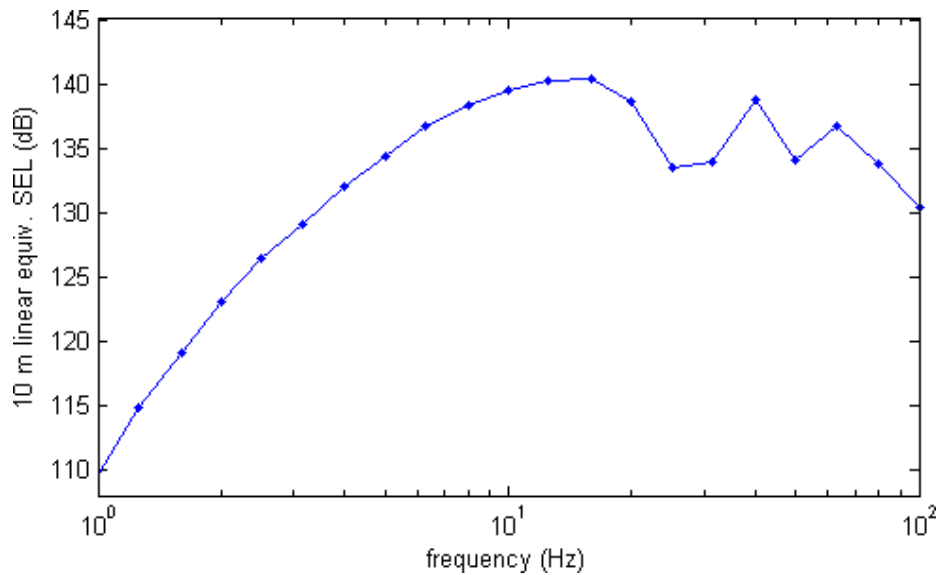

Figure 4.6   Third octave noise emission spectrum for M109. The reference distance R_0 is 10 m.
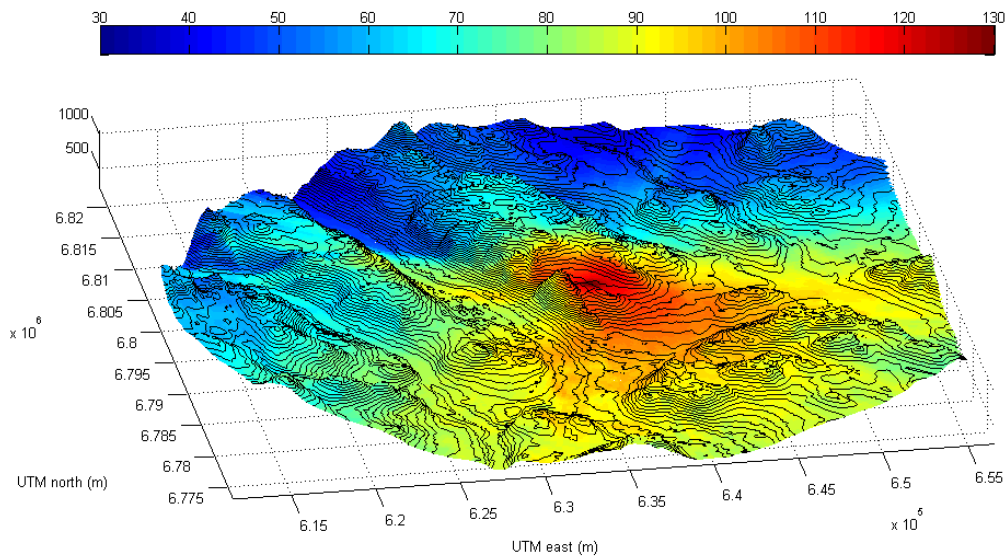
Figure 4.7   Computed sound exposure level from a single firing of M109 in a 25 km radius. Note that the topography is exaggerated.

causing higher sound levels in the downwind direction. Terrain is very important, as is particularly evident in the Northwesterly quadrant with respect to the source, where a narrow strip with rather less attenuation is due to a small valley close to the source. In order to illustrate the variation with frequency we fix the range at 15 km, and plot relative sound level as a function of propagation direction and frequency in Figure 4.5. Attenuation increases with frequency, often with a fairly clear cut-off frequency that varies between 2 and 100 Hz according to direction.

The typical usage of the PE method output is to predict the SEL from a specific source using the formulas (2.2)-(2.3). As an example, we consider one of the noisiest weapons of the Norwegian defence, the M109, a 155 mm howitzer. Its noise emission spectrum is described in [5], see Figure 4.6. A map of the SEL from the M109 is shown in Figure 4.7. We see strong effects of weather and terrain. Small scale details due to interference patterns, which are very prominent in the single frequency map in Figure 4.4, are hardly visible because they are averaged out and because lower frequencies dominate.

The computation time for producing the reference noise maps is shown in Figure 4.8. We show the cumulative time, i.e. the computing time from the lowest up to the given frequency. The effect of adaptive range truncation is illustrated also: Up to 100 Hz the cost is reduced by about one third. The SEL from M109 after range truncation is compared with the untruncated data in Figure 4.9. The maps look practically the same, except in some areas in the Northwest that has an SEL less than about 70 dB.

In Figure 4.9, no Matlab toolboxes were used. We have also tried using 4 processor cores in parallel, using the 'parfor'-construct of the Matlab parallelisation toolbox. Its syntax is conveniently
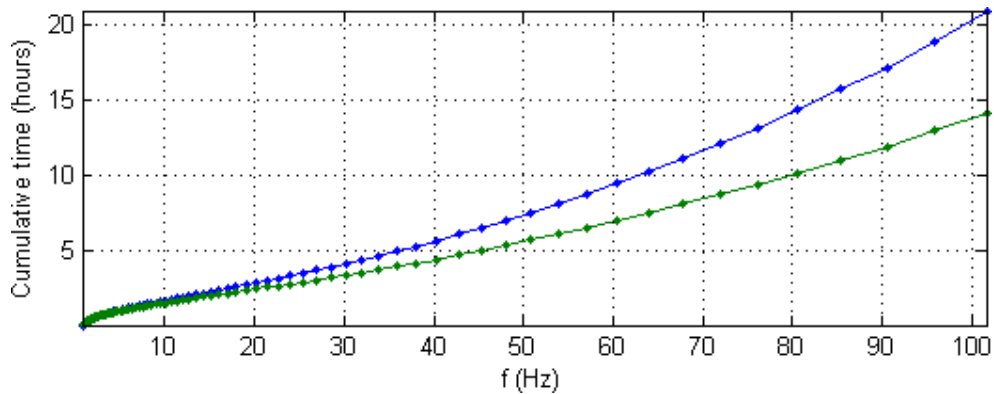
Figure 4.8   Cumulative computational cost by frequency in blue. The sampling is for 12th octaves and for 360 directions. The green line shows the time with range truncation using $L_{\min} = -100\ dB$ and $z_e = 1\ km$.
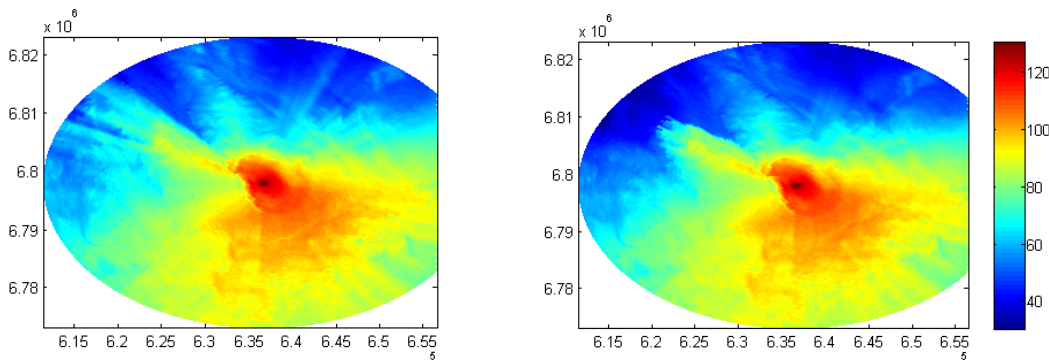

Figure 4.9   Sound exposure level from a single firing of M109. Right: reference solution. Left: range truncated solution.

similar to a regular 'for'-loop, except that one can not rely on the loop elements to be executed in a predictable order. It was the loop over directions that was run in parallel, then there was an external loop over frequencies. We might have expected a speed-up of 4 times compared to standard Matlab, but the actual speed-up was a little more than 3 times. The reason may be that the standard linear algebra routines already take some advantage of the multiple cores.

4.3   Postprocessing

Figure 4.10 demonstrates the postprocessing idea from section 3.4. We show relative sound level as a function of range for selected frequencies. As expected, the narrower minima are smoothed out by postprocessing, and also the local maxima are largely retained. Note that shadow regions due to topography may be smeared by this procedure even though they are more predictable than interference patterns. Hence, we included the terrain profile in the figure.
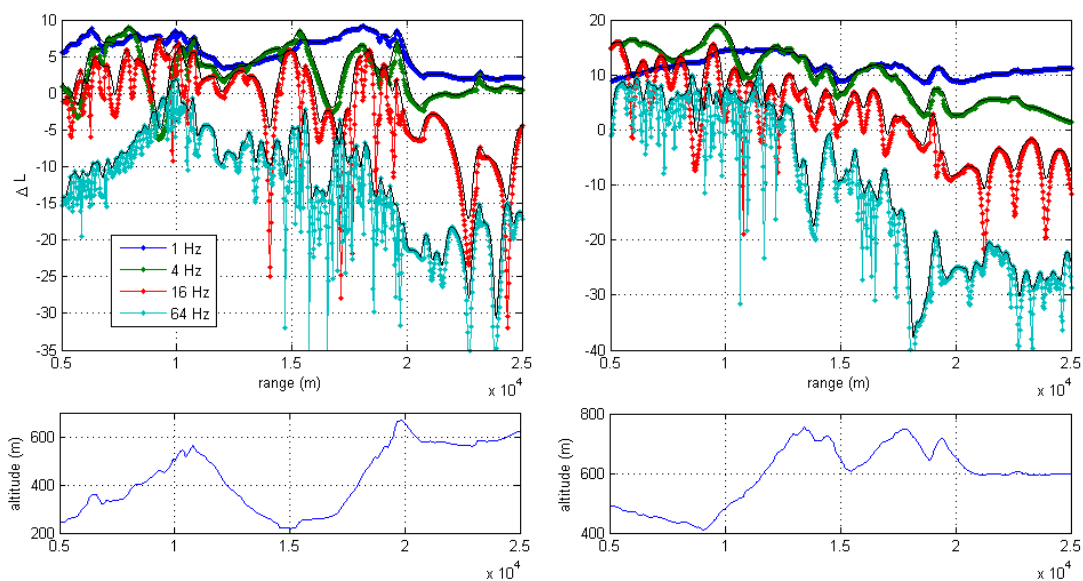
Figure 4.10   Calculated (dots) vs. postprocessed (black lines) sound levels for four frequencies. The propagation directions are 225° (SW, left) and 135° (SE, right). The terrain profiles are shown underneath.
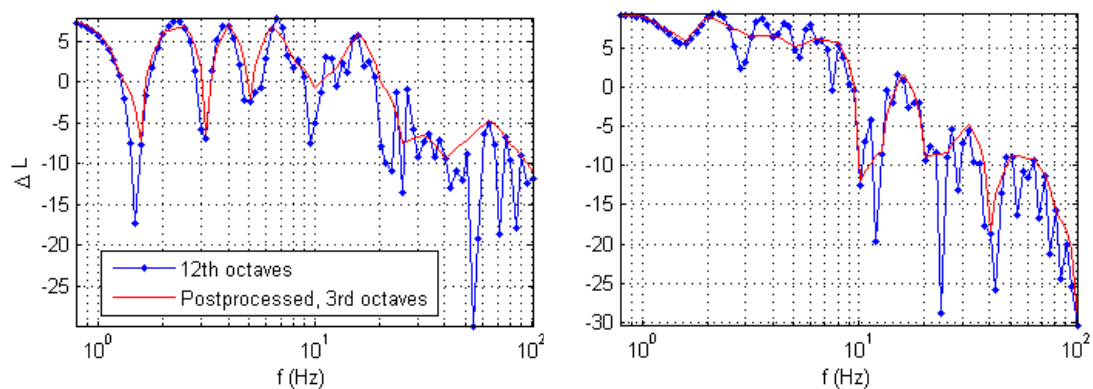

Figure 4.11   Sound level spectrum at 15 km range in the SW (left) and SE (right) directions.
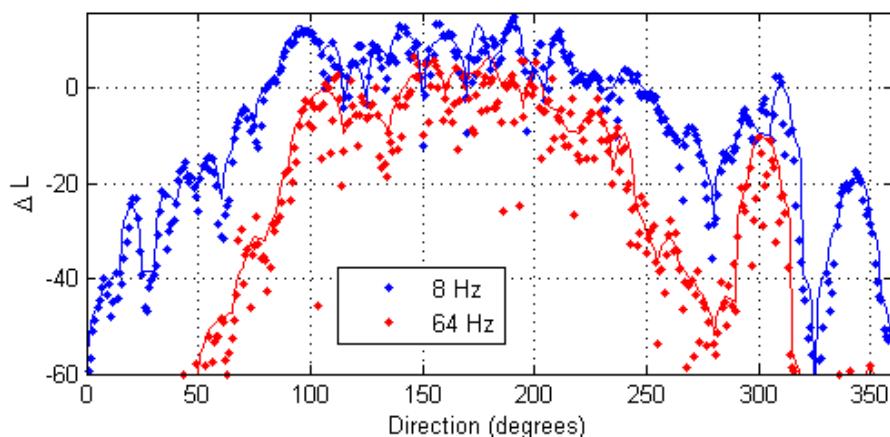
Figure 4.12   Sound level along a circle of radius 15 km. The solid lines are postprocessed, sampled at 72 directions, and then p_f^2 is interpolated linearly.

4.4   Directional and frequency sampling

The reference solution with 360 directions and twelfth octaves is expensive to calculate. Could fewer samples be more cost-efficient? In this section we compare the reference solution to a calculation based on sampling over third octaves in 72 directions. This would reduce computational time by about a factor of 20.

Figure 4.11 illustrates how ΔL varies with frequency in two locations. There are quite narrow minima in the spectrum caused by interference. In these plots, we also include postprocessed data as described in Section 3.4 sampled at third octaves. The postprocessing smooths out some of the interference minima. Figure 4.12 shows that there is also a lot of structure in the directional dimension. The 15 km range is considered, meaning that there is about 260 m between each sample point. Postprocessed data are included with 72 samples instead of all 360. They seem to provide a reasonable interpretation of the data.

The real test for directional and frequency sample rates is to predict broadband noise from a given weapon. Figure 4.13 shows SEL from M109 computed at a reduced sample rate and postprocessed. Differences with the reference solution are subtle. In Figure 4.14 the difference in SEL is plotted. As expected, some shadowing effects are not accurately reproduced due to the missing propagation directions. In the southern region where sound levels are most significant, there are spots where the low resolution mapping yields up to about 5 dB lower SEL. This is caused by the frequency sampling, as is evident from Figure 4.15, where only the frequency sampling varies (i.e. all 360 directions were sampled). No post-processing was used in Figure 4.15, hence the magnitude and size of the spots are bigger.

To conclude this section, the reduced sampling obviously speeds up noise mapping, and on the large scale, and for many practical purposes, the noise maps are as good as the fully resolved maps. It appears that lowering the number of directions results in localised errors, hence some adaptive
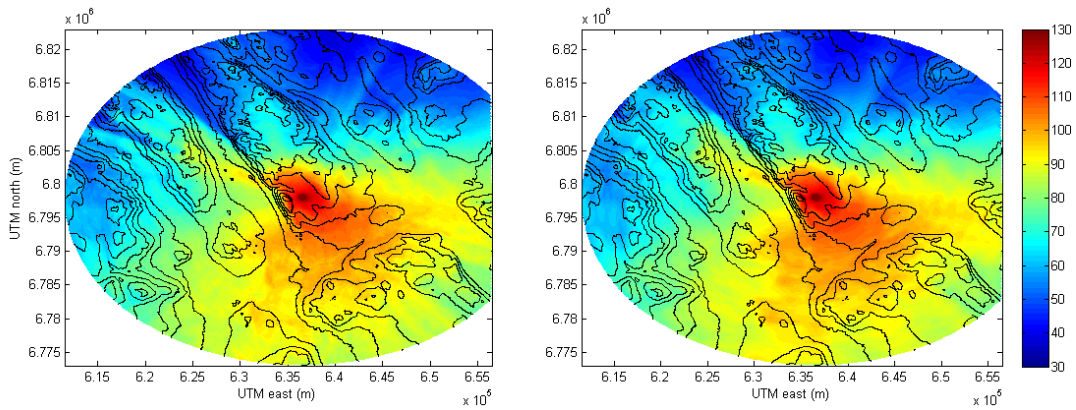
Figure 4.13   M109 SEL. Left: 12th octaves, 360 directions L_{full}. Right: Postprocessed, 3rd octaves and 72 directions, L_{pp}.
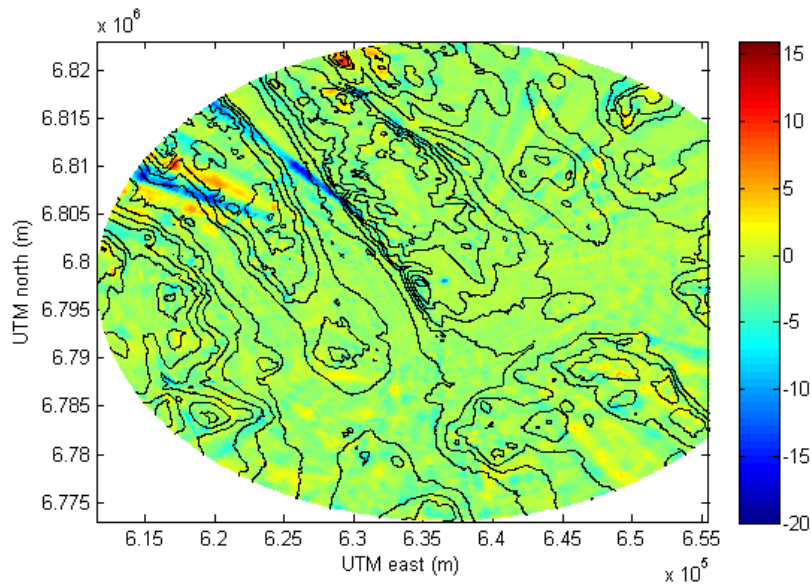

Figure 4.14   The difference $L_{full} - L_{pp}$ between the SELs in Figure 4.13.

approach to directional sampling is probably optimal. Lowering the frequency sampling rate may result in localised errors due to interference patterns. This can be improved with post-processing, and likely represents unpredictable phenomena in any case. Because of this inherent uncertainty, exactly how to postprocess the data is not easily decided.

4.5   Fast mapping for 1-25 Hz.

The frequencies 1-25 Hz are considered especially challenging for Milnoise, therefore it is worthwhile looking at this band isolatedly. The cost of computing the reference solution up to 25 Hz on our four processors is about one hour. As a quicker alternative, we tried using third octaves and only 36 evenly distributed directions. This computation took 4 minutes and 40 seconds without parallelisation. The resulting difference in the M109 SEL, compared to the fully
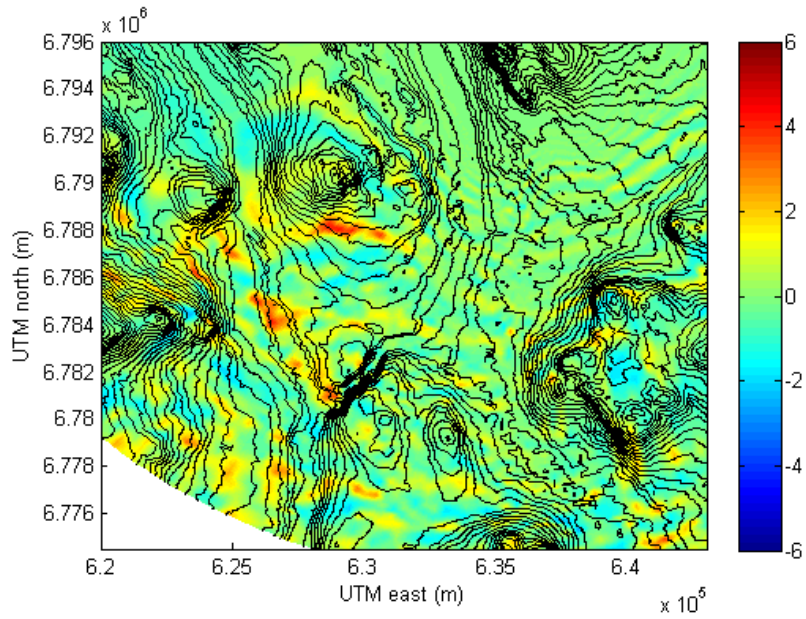
Figure 4.15   The difference $L_{full} - L_{third}$ in SEL due to third octave vs 12th octave sampling.
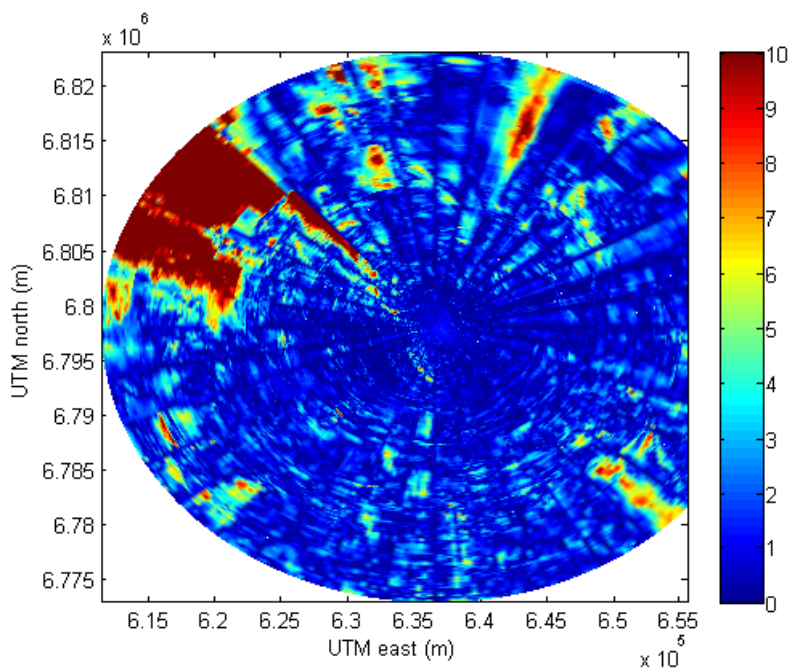

Figure 4.16   The difference between L_{full} and the SEL based on sampling third octaves and 36 directions. Only frequencies up to 25 Hz are considered. The most prominent errors are due to truncation at low sound levels.

resolved case, over the 1-25 Hz band is shown in Figure 4.16. The poor directional resolution is visible as expected, and also the adaptive range truncation causes large discrepancies in the north. But in the downwind regions to the south, where sound levels are large, the error is mostly acceptable. We conclude that the large scale effects of weather, ground effect and (up to a point) terrain are well captured. Hence, this computational strategy is viable if quick results are needed.

5 Summary

We have demonstrated that the PE method can handle a realistic setting from a Norwegian training ground. The implementation is efficient, but the method still has significant computational cost. Reducing cost significantly is not possible without either sacrificing generality or inventing completely new methodology. Because of the cost, the most important potential uses of the code may be to create lookup tables and to validate simpler models. That said, we have shown that for the lowest frequencies, useful noise maps can be created within minutes.

Modelling the atmospheric conditions is a major challenge. This study used a model based on measurements from automatic weather stations. Hence, we lacked data about the atmosphere above 900 m in this study, and we argued that at long distance, this could lead to underestimation of noise. Another potential weakness of the weather model is that it involves no range dependence. Also, uncertainty bounds on the ground admittance values would be very useful in assessing model accuracy, however it is likely that uncertainty in the weather conditions dominates, especially at long range.

References

[1] Keith Attenborough, Ming Li Kai, and Shahram Taherz. *Predicting Outdoor Sound*. Taylor & Francis Ltd, Hoboken, NJ, 2006.

[2] ME Delany and EN Bazley. Acoustical properties of fibrous absorbent materials. *Applied acoustics*, 3(2):105–116, 1970.

[3] LR Hole, Y Gjessing, and T De Lange. Meteorological measurements during Norwegian trials. In *International congress on noise control engineering*, pages 605–610, 1996.

[4] M Huseby, R Rahimi, JA Teland, I Dyrdal, H Fykse, B Hugsted, CE Wasberg, E Aker, R Cleave, F Løvholt, H Olsen, SÅ Storeheier, and Taraldsen. G. Final report: Improvement of the computational methods of the Norwegian defence estates agency for computing noise from the Norwegian defence training ranges. *Norwegian Defence Research Establishment report*, 2008.

[5] Morten Huseby. Noise emission data for M109, 155 mm field howitzer, 2007.

[6] Finn Løvholt. Ground classification. *NGI report*, pages 20071037–5, 2007.

[7] Christian Madshus, Finn Løvholt, Amir Kaynia, Lars Robert Hole, Keith Attenborough, and Shahram Taherzadeh. Air-ground interaction in long range propagation of low frequency sound and vibration - field tests and model verification. *Applied Acoustics*, 66(5):553–578, 2005.

[8] RA Sack and M West. A parabolic equation for sound propagation in two dimensions over any smooth terrain profile: the generalised terrain parabolic equation (gt-pe). *Applied acoustics*, 45(2):113–129, 1995.

[9] Erik M Salomons. *Computational Atmospheric Acoustics*. Springer Netherlands, 2001.

[10] Michelle E Swearingen, Morten Huseby, and Reza Rahimi. *Comparison of Sound Propagation Codes: Milstøy, BNoise and a PE-method*. Forsvarets Forskningsinstitutt, 2009.

[11] G. Taraldsen. The Delany-Bazley impedance model and Darcy's law. *Acta Acustica united with Acustica*, 91(1):41–50, 2005-01-01T00:00:00.

[12] Dan Valente, Lauren M Ronsse, Larry Pater, Michael J White, Roger Serwy, Edward T Nykaza, Michelle E Swearingen, and Donald G Albert. Blast noise characteristics as a function of distance for temperate and desert climates. *The Journal of the Acoustical Society of America*, 132:216, 2012.

[13] K Waagan. Mapping low frequency blast noise using a numerical weather forecast. In Rolf J Korneliussen, editor, *Proceedings of the 38th Scandinavian Symposium on Physical Acoustics*, 2015.

[14] Knut Waagan. Low-frequency long-range atmospheric noise propagation modelling with the PE method. Technical report, Technical Report FFI/RAPPORT-2014/00260, Norwegian Defence Research Establishment, 2014.

[15] Knut Waagan. Numerical prediction of long-range sound propagation - parametric uncertainty and atmospheric models. Technical report, Technical Report FFI/RAPPORT-2014/00577, Norwegian Defence Research Establishment, 2014.

[16] Roger Waxler, Carrick L Talmadge, Shantharam Dravida, and Kenneth E Gilbert. The near-ground structure of the nocturnal sound field. *The Journal of the Acoustical Society of America*, 119:86, 2006.

[17] D Keith Wilson, Edgar L Andreas, John W Weatherly, Chris L Pettit, Edward G Patton, and Peter P Sullivan. Characterization of uncertainty in outdoor sound propagation predictions. *The Journal of the Acoustical Society of America*, 121(5):EL177–EL183, 2007.

[18] D Keith Wilson, Matthew S Lewis, John W Weatherly, and Edgar L Andreas. Dependence of predictive skill for outdoor narrowband and broadband sound levels on the atmospheric representation. *Noise Control Engineering Journal*, 56(6):465–477, 2008.

[19] Cornelis Zwikker and Cornelis Willem Kosten. *Sound absorbing materials*. Elsevier, 1949.

Appendix A   Computational test of the ground model

The Zwikker-Kosten ground model, used in this case study, takes as parameters specific resistivity $\sigma\tau^{-1/2}$ and specific porosity $\Omega\tau^{-1/2}$, with τ denoting tortuosity (see [9, 19]). A common approximation is to let $\tau = \Omega^{-1/2}$, which was used here. The Taraldsen-Darcy model [11] adds an additional simplification in that $\Omega\tau^{-1/2}$ is given as a function of $\sigma\tau^{-1/2}$ based on a fit to the one-parameter Delany-Bazley model [2]. The Delaney-Bazley model is widely used in outdoor acoustics but incorrect at low frequencies. Hence the curve fit in [11] is performed in the applicability range. A summary of these models and others is in [1]. The two impedance models are compared in Figure A.1 for the frequencies 10 and 100 Hz. For the harder classes 6 and 7, Taraldsen-Darcy is not really applicable, since the estimated porosities are unrealistically large.

Figure A.2 shows the effect on sound levels due to the two ground models. The most common ground class (4) is considered, and there is constant effective sound speed and flat topography. Up to about 10 Hz, the propagation approximates a standard full reflection, while above 10 Hz the Taraldsen-Darcy model gives more ground loss by up to about 10 dB. We also compared the two models for a transect from the Rena case study (the same as in Section 4.1). Again, Taraldsen-Darcy gave more damping, as can be seen in Figure A.3.
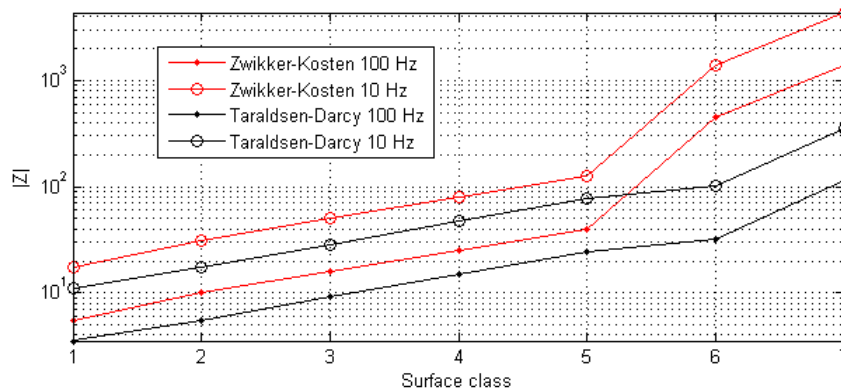

Figure A.1   Comparison between two ground models: Zwikker-Kosten (red), Taraldsen-Darcy (black). The frequencies $f = 10$ Hz (circles) and 100 Hz (dots) are shown for each NGI surface class.

Appendix B   Computational test of range data reduction

As described in Section 3.1, the range dependent data are reduced prior to calculating sound propagation because it is more efficient. Figure B.1 shows a comparison between noise calculation output with and without the reduction. Three range dependent quantities are reduced, namely ground altitude H, ground impedance Z and effective sound speed c. The plot of relative sound level shows that the error due to the reduction is acceptable. There are some localised discrepan-
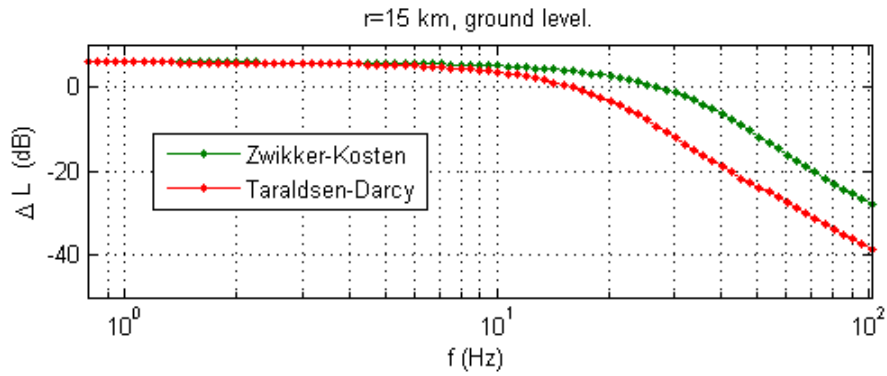
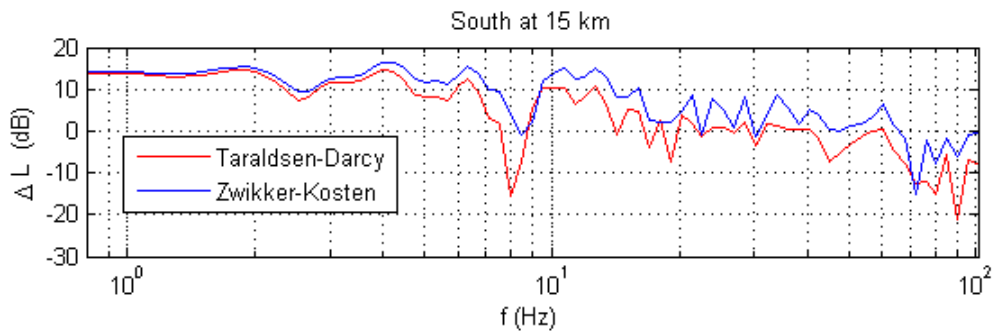*Figure A.2   Relative sound level at r=15 km, z=1.5 m for ground class 4. Flat topography and no refraction.*

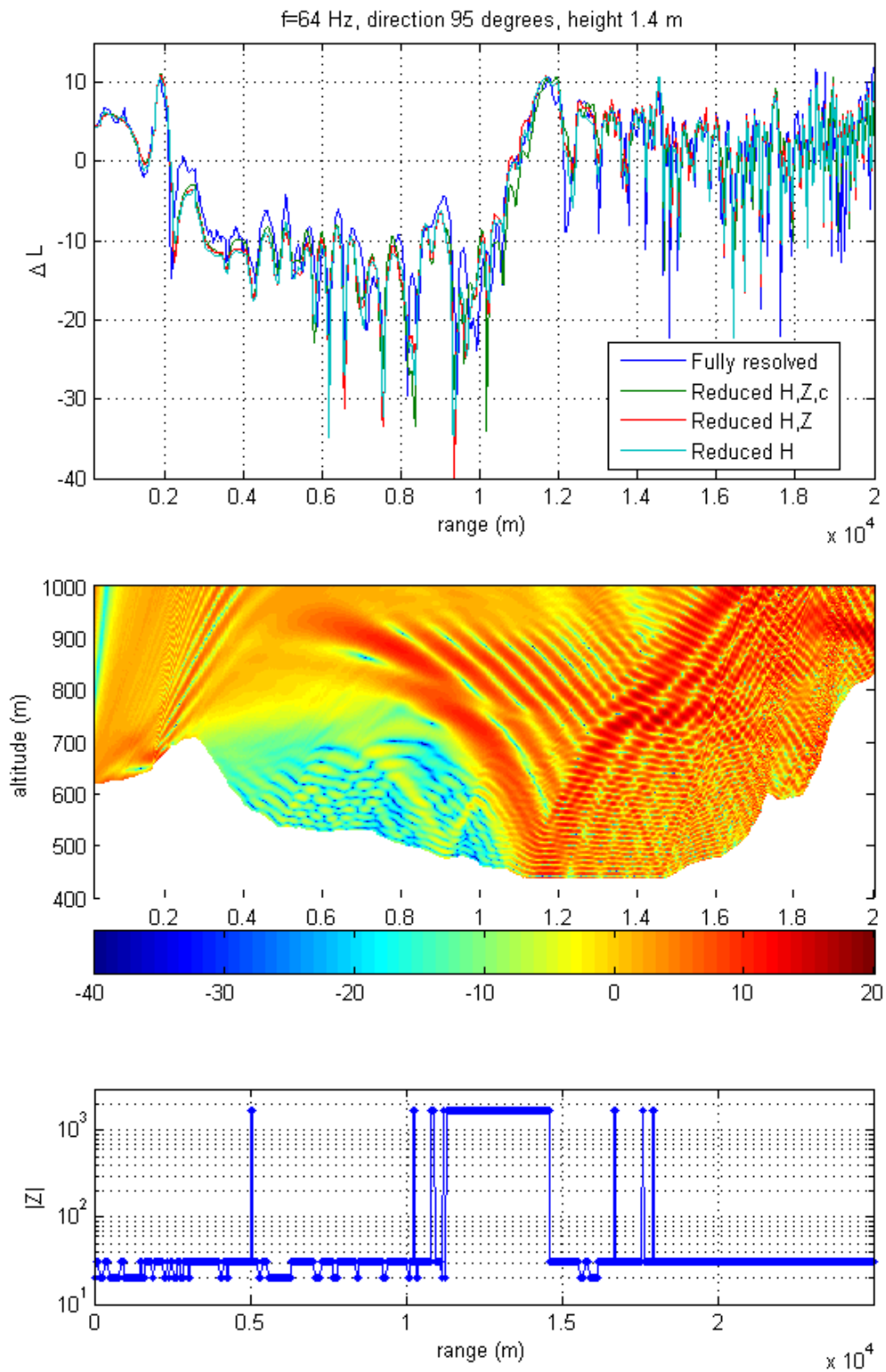*Figure A.3   Relative sound level at r=15 km, z=1.5 m for ground class 4. Flat topography and no refraction.*

Figure B.1   Test of the range reduction algorithm: Top: Relative sound levels for 64 Hz. Middle: Relative sound level by z and r in the unreduced case. Bottom: Unreduced absolute values of ground impedance.
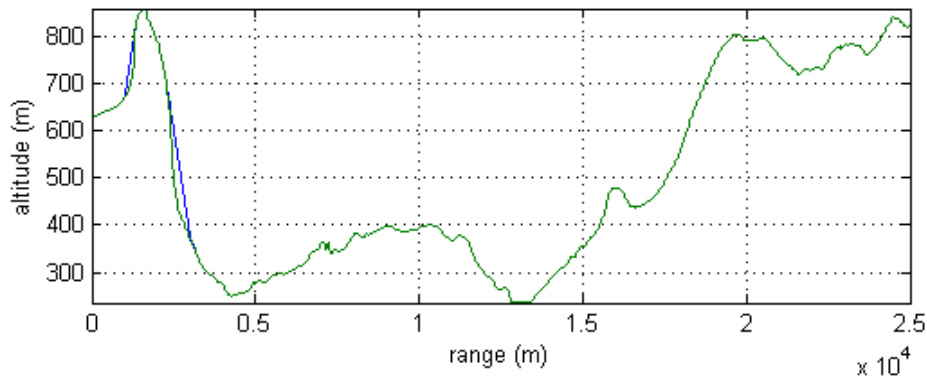
Figure C.1   Topography profile along the 257° direction. The profile after steepness reduction is drawn in blue.

cies of a few dB. These are mostly due to the representation of topography, while the reduction of Z and c has less impact.

Appendix C   Computational test of steepness reduction

The steepness reduction algorithm of section 3.2 is necessary for the stability of the numerical propagation algorithm. Hence, noise levels for the steep slopes are not available for comparison. Instead, in order to get some idea of the significance of this part of the noise mapping algorithm, we resort to perturbing the maximum slope C in (3.1). The actual slopes in the maps reach a maximum value of about 1.94 in the 257° direction some 2 km from the source. We consider that propagation direction, as it represents a worst case for the noise mapping study in this report. The topography profile is shown in Figure C.1. We performed calculations with a maximum slope $C = 0.5$ and with $C = 0.45$. One would hope for these two calculations to give much the same result away from the reduced slopes. Looking at the difference between the two in Figure C.2, we note a patchwork of large discrepancies even at far range. However, when comparing to the plot of ΔL in the same figure, we note that the discrepancies are related to interference minima, which are in any case known to be very sensitive to perturbations. This test therefore indicates that the reduced slopes provide a reasonable approximation away from the hillsides.

Appendix D   Surface class labels

We received a map from Sintef of the surface classification. There are seven surface classes (named A-G or 1-7). In this map, the class labels did not coincide with the NGI labels. One reason is that the Milnoise low frequency module, for which this map was created, includes special treatment of built-up areas. We assigned the built up areas to surface class F. Water bodies were labelled with 0. The interpretation of the surface class table is summarised in Table D.1.
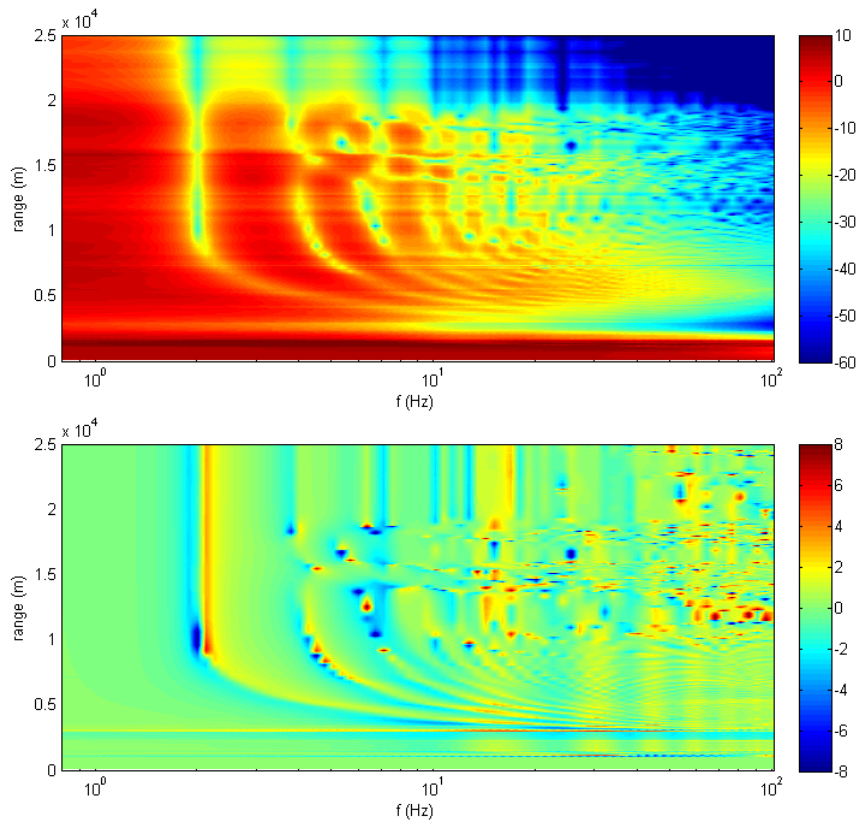
Figure C.2   Top: Relative sound level $\Delta L|_{C=0.5}$ as a function of frequency and range. Maximum slope C was (as indicated) set to the default value 0.5. ΔL was evaluated at ground level. Bottom: The difference $\Delta L|_{C=0.5} - \Delta L|_{C=0.45}$.

Table value	NGI surface class
0	G
1	A
2	B
3	C
4	D
5	E
6	F
14	F

Table D.1   Interpretation of surface class labels.

Appendix E Geographical data treatment

We use a digital elevation model with a uniform grid given over latitude and longitude. The resolution is approximately 30×30 m. The coordinates were transformed to UTM32. The ground surface classification map is given on a 25×25 m grid in UTM32 coordinates.

These two data sets are convenient to have in the same coordinates and grid. We choose the surface data 25×25 m grid as the common reference. For the elevation data we use piecewise bilinear interpolation. The noise prediction calculations are carried out along transects that rarely coincide nor co-align with this grid. Hence further interpolation is required. Bilinear interpolation is again chosen for the elevation data. For the ground classes we use nearest neighbour interpolation.

An alternative approach for the ground class data is to first look up admittance values, and then interpolate. This approach was abandoned due to being more computationally intensive, more complicated to implement, and having seemingly insignificant impact on results. The assignment of impedance values onto a large grid of ground class values can be performed efficiently in Matlab using 'uniquefication' and logical indexing, for which we may use the following code:

```
function Z = classToZ(f, gclassline )
Z=Inf*gclassline;
classlist=unique(gclassline);
for ii=1:length(classlist)%Loop to assign Z-values
    Zunique=Zlookup(f,classlist(ii));
    Z(gclassline==classlist(ii))=Zunique;
end
end
```

Note that Z is only looked up once for each distinct class value (by calling *Zlookup*). It turned out to be much more efficient to use logical indexing directly instead of temporarily storing a list of indexes. The above code is mostly used with a single vector of class values as input, but also works for a matrix.

Appendix F Noise mapping algorithm

Given a source location, noise mapping is performed as follows:

1. Elevation data and ground classification along each radial transect are computed and saved to files. Slopes are reduced before saving.
2. For each frequency we do the following:

   (a) For each transect, run the main PE calculation. Then store values of relative sound level ΔL at given heights (we chose 0, 1.5 and 4 meters) above ground in an array.

   (b) Write the stored data to a separate file for each frequency.

The inner loop, i.e. the loop over propagation directions is convenient to execute in parallel. From Matlab's parallel toolbox, we can utilize a *parfor* loop for this on a single multicore processor.

Each PE calculation incorporates the following steps:

1. Read in some basic parameters such as grid resolution from a file. They include source height, grid resolution, computational domain height.
2. Read in and process the elevation and ground class data. Impedance values are assigned, and data is reduced to 'range sections' of constant slope and impedance.
3. Read in the weather data. The weather profile is fixed as a function of height above ground for each range section.
4. Generate start-up data
5. Generate sparse matrix structures that approximate the differential operators. It saves time to only perform this task once.
6. The main loop: Loop over the range sections, and calculate Ψ.
7. Calculate geometric attenuation across the grid, which requires reading in the elevation data again. Then, finally, relative sound level ΔL can be calculated.

For each range section, the algorithm can be broken down further:

1. Set the output range values to be uniformly spread with a distance l/N_{out} where l is the length of the range section and N_{out} is a given number of output points.
2. Set the range step size Δr such that it is smaller than Δz, and such that there is an integer number of range steps between each output range value.
3. Generate the matrices M_1 and M_2 from [9].
4. Perform an LU factorisation of M_2.
5. Perform the first range step using Gaussian elimination. The reason is that the boundary condition, involving Ψ_r, can only be calculated to first order in the first range step.
6. Perform the remaining range steps using the LU factorisation, i.e. back-substitutions.

Typically, a majority of computational time is spent doing back-substitutions.